Benchmarking the GENE and GYRO Codes through the Relative Roles of Electromagnetic and E×B Stabilization in JET High-Performance Discharges

R. Bravenec,[1] J. Citrin,[2,3] J. Candy,[4] P. Mantica,[5] T. Görler,[6] and JET contributors[7]

[1]Fourth State Research, Austin, TX

[2]FOM Institute DIFFER – Dutch Institute for Fundamental Energy Research, PO Box 6336, 5600 HH Eindhoven, The Netherlands

[3]CEA, IRFM, F-13108 Saint Paul Lez Durance, France

[4]General Atomics, San Diego, CA

[5]Instituto di Fisica del Plasma ''P. Caldirola,'' CNR, Milano, Italy

[6]Max Planck Institute for Plasma Physics, Boltzmannstr. 2, 85748, Garching, Germany

[7]See Appendix of F. Romanelli *et al.*, Proc. 25th IAEA Fusion Energy Conf. 2014

Abstract

Nonlinear gyrokinetic simulations using the GENE code have previously predicted a significant effect of nonlinear enhanced electromagnetic stabilization in certain JET discharges with high neutral-beam power and low core magnetic shear [J. Citrin *et al*., Phys. Rev. Lett. **111** (2013) 155001, Plasma Phys. Contr. Fusion **57** (2015) 014032]. This dominates over the impact of **E×B** flow shear in these discharges. Furthermore, fast ions were shown to be a major contributor to the electromagnetic stabilization. These conclusions were based on results from the GENE gyrokinetic turbulence code. In this work we verify these results using the GYRO code. Comparing results (linear frequencies, eigenfunctions, and nonlinear fluxes) from different gyrokinetic codes as a means of verification (benchmarking) is only convincing if the codes agree for more than one discharge. Otherwise, agreement may simply be fortuitous. Therefore, we analyze three discharges, all with a carbon wall: a simplified, two-species, circular geometry case based on an actual JET discharge; an L-mode discharge with a significant fast-ion pressure fraction; and a low-triangularity high-β hybrid discharge. All discharges were analyzed at normalized toroidal flux coordinate $\rho = 0.33$ where significant ion temperature peaking is observed. The GYRO simulations support the conclusion that electromagnetic stabilization is strong, and dominates E×B shear stabilization.

Introduction

The scaling of tokamak microturbulence to the plasma β (ratio of plasma to magnetic-field pressure) is of intense interest, due to the need to extrapolate performance to high-β, low-rotation reactors. Extensive research with gyrokinetic simulations has studied electromagnetic stabilization of ion-temperature-gradient (ITG) transport in the linear[1-5] and nonlinear[6-16] regimes. Recent work[11,12] showed through GENE[17] simulations that nonlinear electromagnetic stabilization is dominant over **E×B** flow shear in certain JET discharges with high neutral-beam power and low core magnetic shear. Furthermore, suprathermals (D beam ions, He3 ICRF minority ions) were found to augment the stabilization, explaining the observation of a reduced ion temperature stiffness regime.[18,19] The degree of electromagnetic stabilization is correlated with the proximity of the system to the critical β, β_{crit}, of the eventual electromagnetic instability, due to increased coupling to the shear-Alfven branch.[20] Thus, β/β_{crit} has been shown to be a parameter of merit for the EM-stabilization, with maximum stabilization at $\beta/\beta_{crit} = 1$.[21] Since the primary effect is actually that of $d\beta/dr$, β_{crit} is reduced at higher pressure gradients, including suprathermal

Table 1. Input plasma parameters to the codes. Here ν_{ei} is the electron-ion collision frequency, γ_{ExB} is the E×B shearing rate, $c_s = (kT_e/m_i)^{1/2}$ is the ion sound speed, and r is the flux-surface half-diameter at the elevation of the magnetic axis (a is the value of r at the plasma edge). The other parameters have the usual definitions. Red entries signify notable difference among shots.

Shot	66404	73224	75225
r (m)	0.31	0.36	0.35
a (m)	0.94	0.96	0.94
n_e (10^{19} m^{-3})	2.3	2.95	3.92
T_e (keV)	4.0	3.2	4.8
n_i/n_e	1.0	0.648	0.79
n_{imp}/n_e	0.0	0.025	0.015
$T_i/T_e = T_{imp}/T_e$	1.0	1.0	1.19
$a/L_{ne} = a\ d\ln(n_e)/dr$	-0.924	-0.422	-0.906
$a/L_{ni} = a\ d\ln(n_i)/dr$	-0.924	-0.006	-0.760
$a/L_{nimp} = a\ d\ln(n_{imp})/dr$	-	-0.422	-0.906
$a/L_{Te} = a\ d\ln(T_e)/dr$	-1.65	-2.23	-1.31
$a/L_{Ti} = a\ d\ln(T_i)/dr$	-2.84	-3.56	-2.51

Shot	66404	73224	75225
$R_0(r)/a$	3.03	3.12	3.23
$\Delta = dR_0(r)/dr$	0	-0.14	-0.15
q	1.7	1.74	1.14
$s = r\ d\ln(q)/dr$	0.2	0.523	0.159
κ	1.0	1.26	1.32
$s_\kappa = r\ d\ln(\kappa)/dr$	0	0.030	-0.009
δ	0	0.030	0.036
$s_\delta = r\ d\delta/dr$	0	0.032	00.02
β_e	0.003	0.003	0.018
Z_{eff}	1.0	1.9	1.45
$\nu_{ei}\ a/c_s$	0.015	0.032	0.019
$\gamma_{E\times B}\ a/c_s$	-	0.117	0.073

pressure gradients. Nonlinearly, the further increased stabilization is correlated with a relative increase in the zonal flow growth rate.[22] The exact mechanism for this is still under investigation.

Here we verify these results using the GYRO[23] code, an Eulerian gyrokinetic code like GENE, but which solves for the radial dependencies in real space. This exercise also benchmarks the codes in high-performance regimes. In all cases, we ensure that the input plasma parameters, listed in Table 1, are identical for both codes. In the table, ν_{ei} is the electron-ion collision frequency, γ_{ExB} is the **E×B** shearing rate, $c_s = (kT_e/m_i)^{1/2}$ is the ion sound speed, and r is the flux-surface half-diameter at the elevation of the magnetic axis (a is the value of r at the plasma edge). The other parameters have the usual definitions. Resolution (real and velocity space) is as similar as possible. All simulations use the Miller[24] parameterization for the plasma shape. All analysis takes place at $\rho = 0.33$, where ρ is the minor radius defined as the normalized square root of toroidal flux, and at times that are in the steady-state phase of the discharges.

Shot 66404

We begin with analysis based on low-β JET discharge 66404. To simplify the benchmark for this case, we set the shape to circular, unshifted geometry (still with Miller parameterization), and neglect impurities and fast ions. This isolates the impact of electromagnetic stabilization. Here the GYRO resolution parameters were as follows: the number of passing and trapped grid points was each six with eight energy grid points. The number of grid points in the poloidal direction along a particle orbit was 12 as was the number of blending functions used to discretize the field equations and the radial grid.

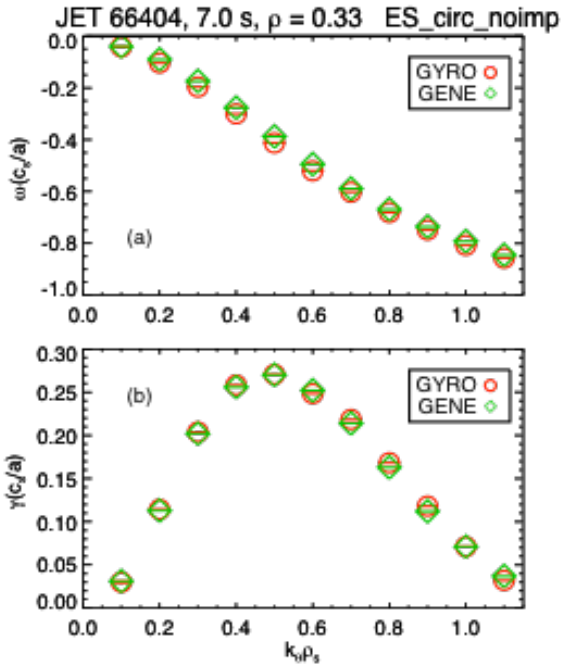

Figure 1. Gyro-Bohm normalized (a) real and (b) imaginary frequencies for the most unstable mode versus normalized wave number for discharge 66404 at t = 7 s and ρ = 0.33, electrostatic.

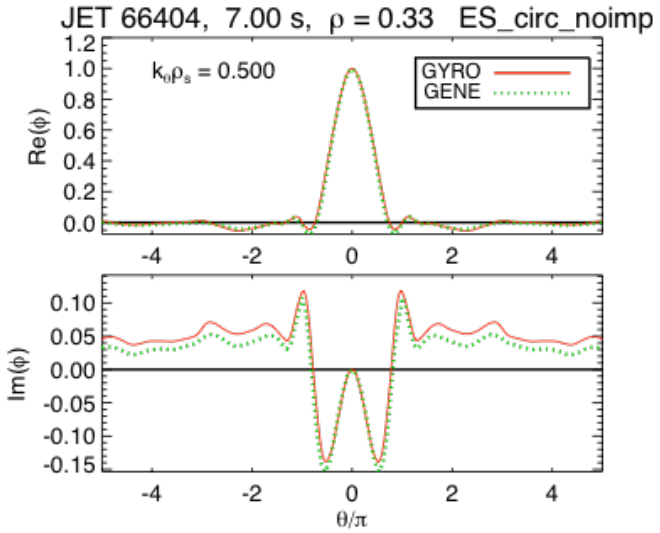

Figure 2. Eigenfunctions of the electrostatic potential for $k_\theta \rho_s$ = 0.5 vs extended poloidal angle for shot 66404 at t = 7 s and ρ = 0.33, electrostatic.

We first present electrostatic results. The linear frequencies of the most unstable modes are shown in Fig. 1, where k_θ is the wave number in the poloidal direction and ρ_s is the ion gyroradius using the ion sound speed. We observe excellent agreement between the codes. The eigenfunctions of plasma potential for $k_\theta \rho_s$ = 0.5 (near the maximum of the growth rate) are shown in Fig. 2, where again the agreement between codes is good. (The differences in the tails of the functions are only ~2% of the peak value.) The negative real frequencies correspond to the ion diamagnetic direction and the eigenfunction parity is ballooned. These are signatures of ion-temperature-gradient (ITG) modes.

Next we turn to nonlinear simulations. Here the resolutions in velocity space for GYRO are the same as for the linear runs. The radial extent of the simulation box was 125 ρ_s while the poloidal extent was 170 ρ_s. The number of poloidal modes was 48 with the smallest nonzero mode being $k_\theta \rho_s = 0.05$. The GENE values were the same.

Found in Table 2 are the gyro-Bohm-normalized fluxes averaged over the period beyond the initial transients of the simulations. This period (hundreds of a/c_s) is many times the underlying

Table 2. Gyro-Bohm normalized time-averaged fluxes for shot 66404, electrostatic. From left to right are the electrostatic electron, ion, and impurity ion energy flux densities, the electromagnetic electron energy flux density, and the electron and ion particle flux densities.

	$Q_e/Q_{e,gB}$	$Q_i/Q_{e,gB}$	$Q_{imp}/Q_{e,gB}$	$Q_{e,B\perp}/Q_{e,gB}$	$\Gamma_e/\Gamma_{e,gB}$	$\Gamma_i/\Gamma_{e,gB}$
GYRO	5.12 ± 0.53	19.3 ± 2.27	—	—	1.36 ± 0.16	1.36 ± 0.16
GENE	4.44 ± 0.43	18.9 ± 1.91	—	—	1.05 ± 0.12	1.05 ± 0.12

correlation time of the fluctuations. The gyro-Bohm flux densities are $Q_{e,gB} = n_e c_s T_e (\rho_s/a)^2$ and $\Gamma_{e,gB} = Q_{e,gB}/T_e$. In this case the impurity ion flux and electromagnetic flux are zero by definition. The uncertainties, representing the inherent intermittency of the fluxes, are the standard deviations from the means. The fluxes versus time are shown in Fig. 3 where the mean values and the averaging window are denoted by the dashed lines. We observe good agreement between the codes when taking the uncertainties into account.

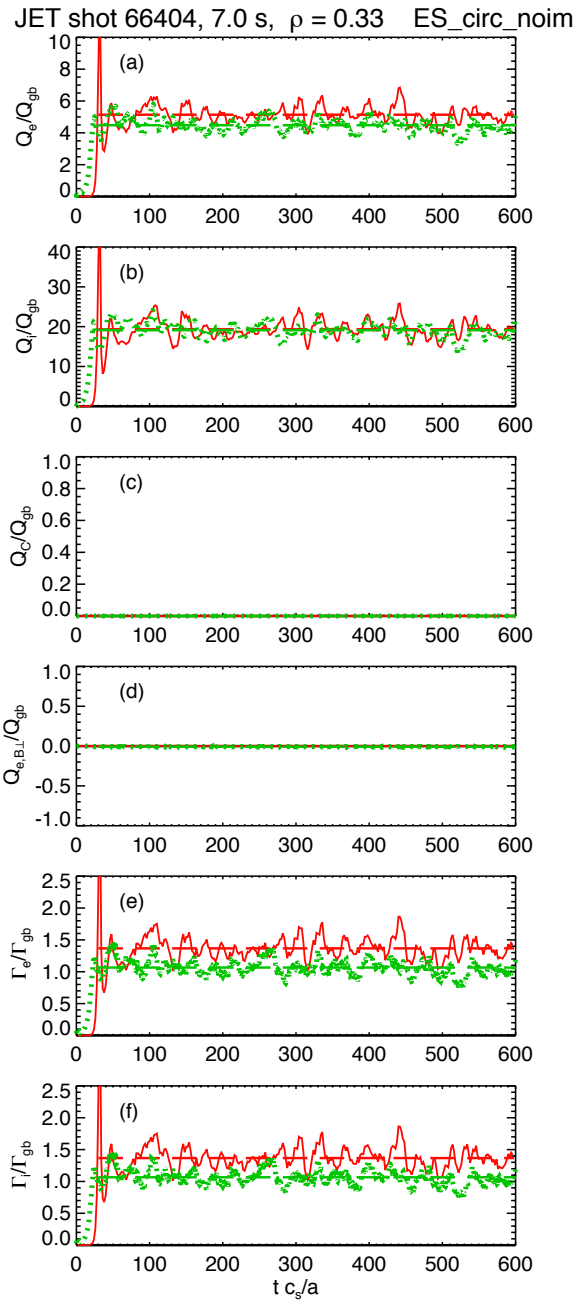

Figure 3. Gyro-Bohm-normalized (a) electron, (b) main ion (D), and (c) impurity ion (C^{6+}) electrostatic energy fluxes, (d) electron energy flux from vector B fluctuations, and (e) electron and (f) main ion electrostatic particle fluxes for JET discharge for discharge 68404 electrostatics. GYRO in solid red (—) and GENE in dotted green (·····). Time is normalized to the sound transit time a/c_s. Straight dashed lines indicate averages over the time range shown.

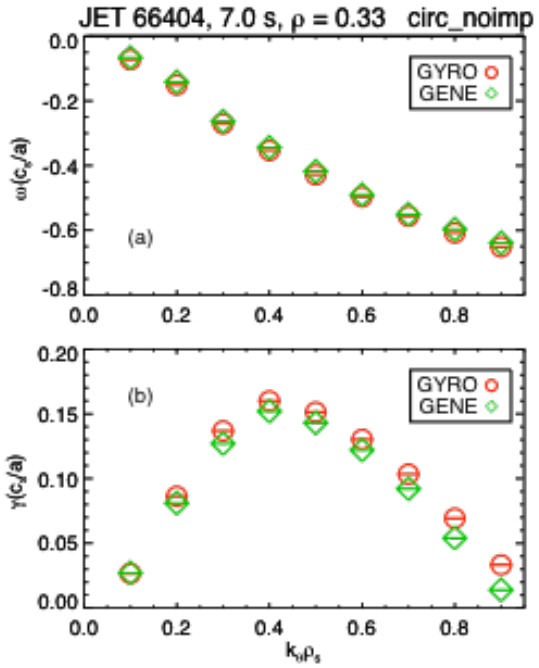

Figure 4. Same as Fig. 1 except including perpendicular electromagnetic fluctuations

Next we allow for fluctuations in the perpendicular component of the magnetic field, i.e., electromagnetic (EM) effects. This is the first benchmarking study between GENE and GYRO of the ITG nonlinear

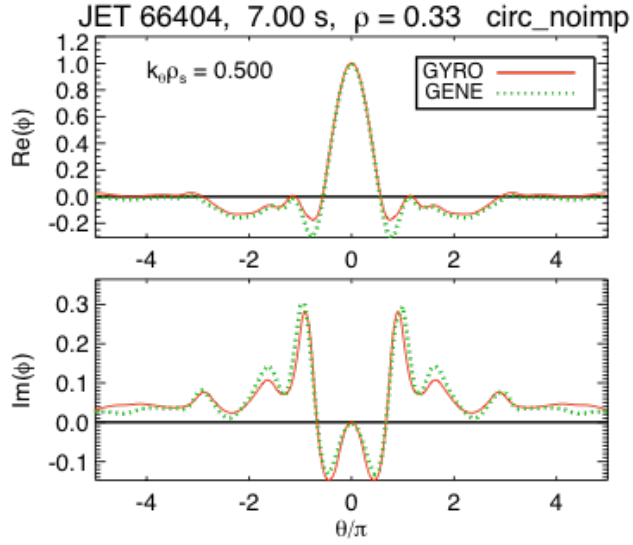

Figure 5. Same as Fig. 2 except including perpendicular electromagnetic fluctuations.

Table 3. Same as Table 2 except including perpendicular electromagnetic fluctuations.

	$Q_e/Q_{e,gB}$	$Q_i/Q_{e,gB}$	$Q_{imp}/Q_{e,gB}$	$Q_{e,B\perp}/Q_{e,gB}$	$\Gamma_e/\Gamma_{e,gB}$	$\Gamma_i/\Gamma_{e,gB}$
GYRO	3.08 ± 0.76	8.36 ± 2.01	—	-0.08 ± 0.13	0.88 ± 0.24	0.88 ± 0.24
GENE	2.09 ± 0.43	6.53 ± 1.21	—	-0.16 ± 0.09	0.55 ± 0.13	0.55 ± 0.13

electromagnetic stabilization physics. The results are shown in Figs. 4 and 5 and Table 3. The linear frequencies are seen to be in good agreement except near the stability boundary (around $k_\theta \rho_s \sim 1$). This indicates the codes disagree in the exact value of the boundary. Note the reduction in the growth rates from Fig. 1 of order 40%. The eigenfunctions are similarly in agreement except in the amplitude of the small oscillations. The fluxes, however, given in Table 3 are significantly different between the two codes, although the error bars do overlap. Nevertheless, upon comparisons with Table 2, we note that both codes agree on a substantial reduction of the fluxes when including EM effects: 40% - 60% depending on the code and the specific flux — greater than the reduction in the growth rates. It is interesting to note that the fluxes directly attributed to EM fluctuations are very small, i.e., the reductions in fluxes due to EM fluctuations manifest themselves primarily through the electrostatic fluxes.

Shot 73224

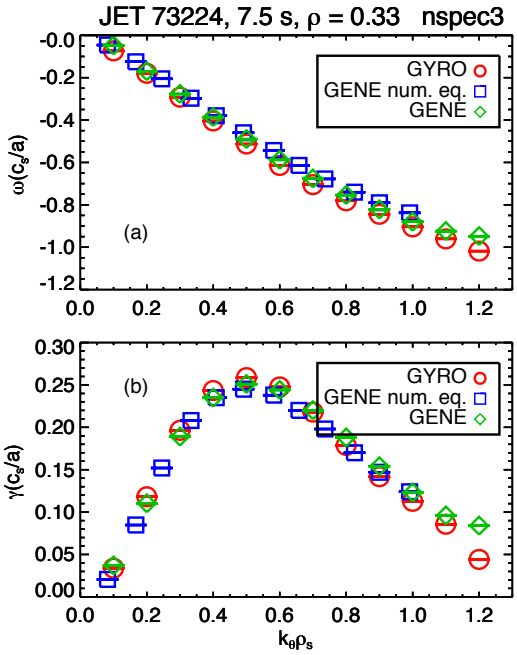

Figure 6. Same as Fig. 4 except for discharge 73224 with three dynamic species. Also shown are GENE results using a numerical equilibrium.

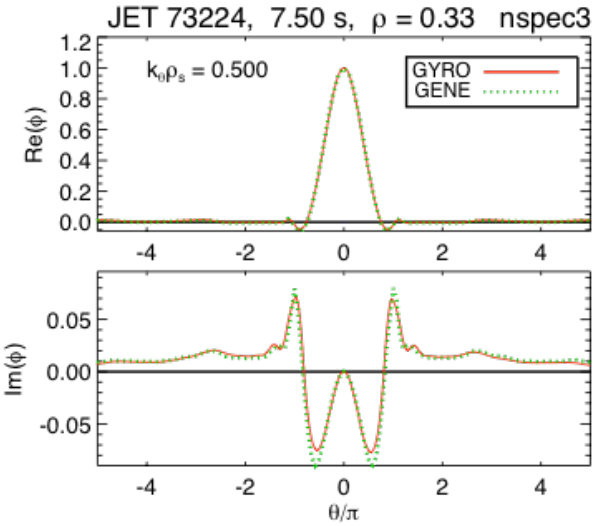

Figure 7. Same as Fig. 5 except for discharge 73224 with three dynamic species.

Next we consider the JET discharge 73224, an L-mode discharge with a significant fast-ion pressure fraction. We examine what role suprathermals, namely, D beam ions and He3 ICRF minority ions, play in the electromagnetic stabilization of ITG modes. Electromagnetic results for only three dynamic species (main ion, electron, carbon) are shown in Figs. 6 and 7 and Table 4. Again, the linear frequencies agree well between codes except approaching the stability boundary, here near $k_\theta \rho_s \geq 1.2$. As an aside, we investigate the validity of the Miller parameterization of the shape. Also shown in Fig. 6 are the linear frequencies from GENE using a numerical equilibrium. We see the numerical results are practically indistinguishable from the Miller results, which is expected at this radius for which shaping is weak. The eigenfunctions are in excellent agreement and the fluxes are in fair agreement considering the error bars.

We now consider the effects of the fast particles, namely, D beam ions and He3 ICRF minority ions. The electromagnetic results are shown in Figs. 8 – 10. The linear frequencies and

Table 4. Same as Table 3 except for discharge 73224 with three dynamic species

	$Q_e/Q_{e,gB}$	$Q_i/Q_{e,gB}$	$Q_{imp}/Q_{e,gB}$	$Q_{e,B\perp}/Q_{e,gB}$	$\Gamma_e/\Gamma_{e,gB}$	$\Gamma_i/\Gamma_{e,gB}$
GYRO	9.45 ± 2.97	24.8 ± 8.06	0.70 ± 0.21	0.65 ± 0.43	1.64 ± 0.67	1.60 ± 0.66
GENE	7.32 ± 1.82	20.8 ± 5.42	0.70 ± 0.17	0.61 ± 0.29	1.19 ± 0.36	1.16 ± 0.37

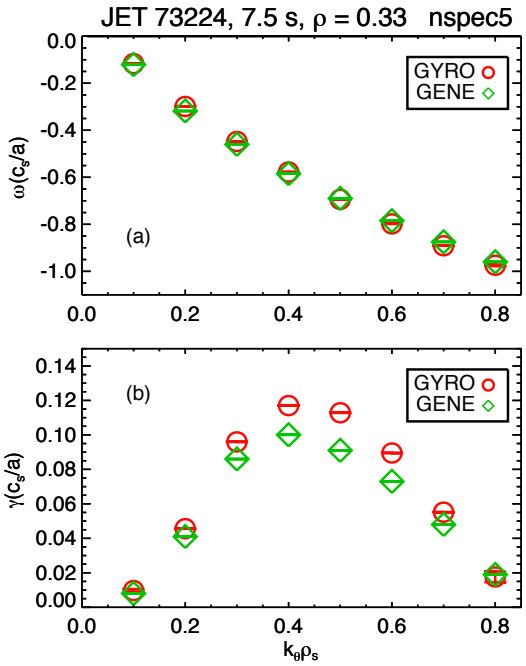

Figure 8. Same as Fig. 6 except with five dynamic species.

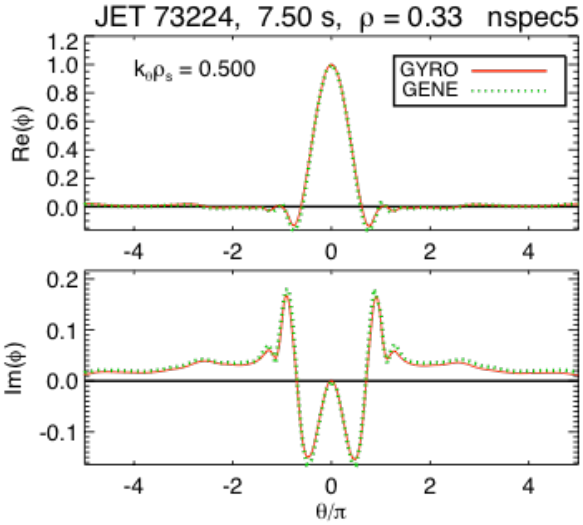

Figure 9. Same as Fig. 7 except with five dynamic species.

the eigenfunctions are in excellent agreement between codes except that the peak growth rate predicted by GYRO is about 10% higher than that from GENE. The fluxes are displayed in Fig. 10 rather than in a table to show their time dependences. We see that both codes predict time-decaying fluxes. Due to the significant computational cost of these runs, we did not continue the runs to determine if the fluxes decay to zero or if they settle on a very small average level. In either case, the conclusion that fast particles strongly contribute to the EM stabilization is clear, and that they produce at least a factor 20 reduction in the fluxes when compared with Table 4. This reduction, due to the diminished ability of ITG-like modes to drive heat fluxes, is much larger than the decrease in the peak growth rate (factor ~ 2.5) from that in Fig. 6. Although not shown, we should note that EM stabilization is much less for the three-species case than for the five-species case.

Table 5. Same as Table 4 except including E×B flow shear.

	$Q_e/Q_{e,gB}$	$Q_i/Q_{e,gB}$	$Q_{imp}/Q_{e,gB}$	$Q_{e,B\perp}/Q_{e,gB}$	$\Gamma_e/\Gamma_{e,gB}$	$\Gamma_i/\Gamma_{e,gB}$
GYRO	4.68 ± 0.50	12.0 ± 1.34	0.56 ± 0.06	0.77 ± 0.15	0.69 ± 0.12	0.35 ± 0.11
GENE	4.92 ± 0.67	14.4 ± 1.93	0.71 ± 0.09	0.44 ± 0.15	0.73 ± 0.14	0.40 ± 0.12

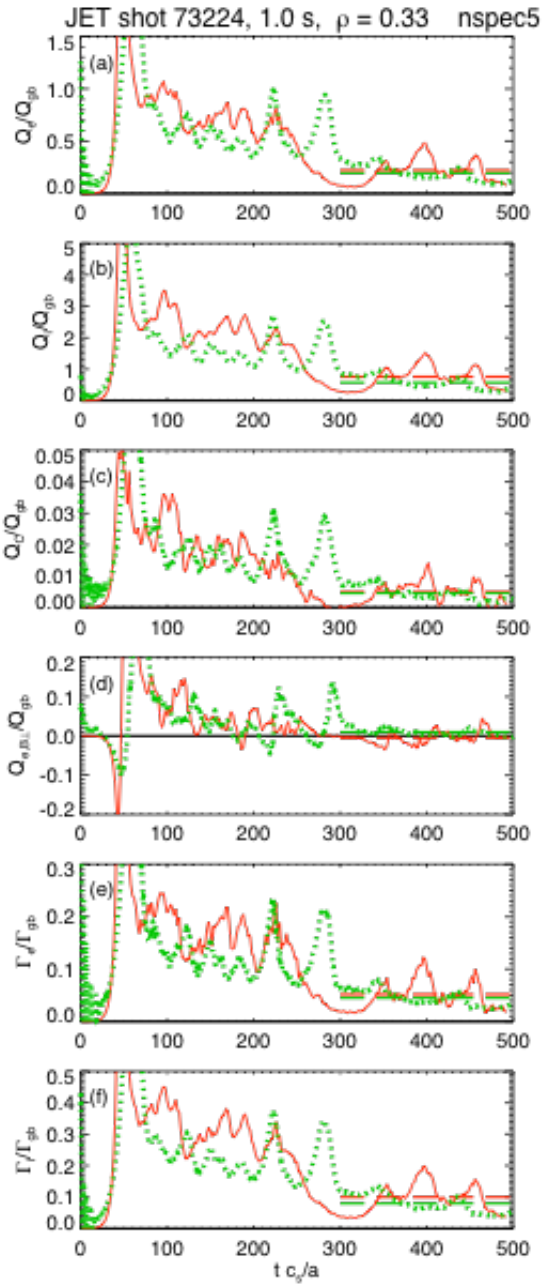

Figure 10. Same as Fig. 3 except for discharge 73224 with five species.

We now examine the impact of **E×B** flow shear on the fluxes. Results are shown in Table 5 for three dynamic species, where the electromagnetic stabilization is significantly weaker compared to the five species case. We first observe good agreement between the codes. Comparing with Table 4 we see about a factor of 1.5 reduction in the fluxes due to **E×B** flow shear. This is a much less significant reduction compared to including electromagnetic effects.

Shot 75225

We next examine the high-β hybrid discharge 75225 including dynamic beam ions. Electrostatic results are presented in Figs. 11, 12, and Table 6. Agreement of the linear frequencies is again good, but there are some differences in the eigenfunctions. The fluxes are in good agreement considering the error bars. Electromagnetic results are found in Figs. 13, 14, and Table 7, where we include fluctuations in the parallel component of the magnetic field. We note that parallel magnetic fluctuations were found to be important only for 75225, due to the

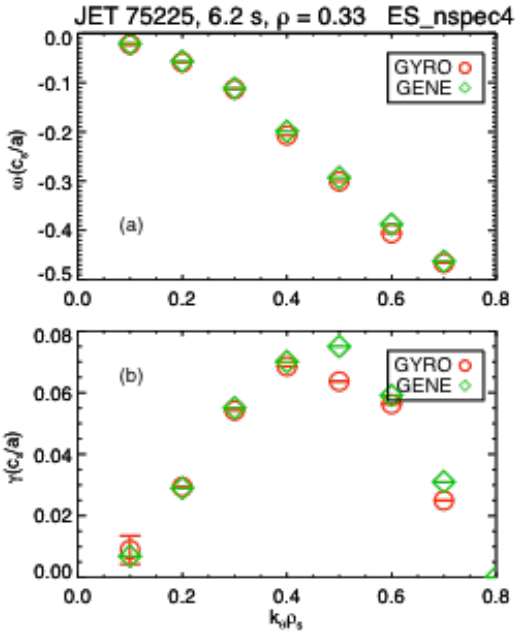

Figure 11. Same as Fig. 1 except for discharge 75225, four dynamic species.

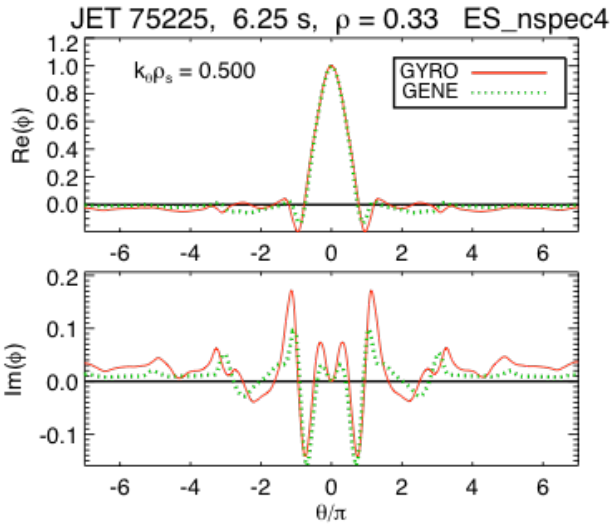

Figure 12. Same as Fig. 2 except for discharge 75225, four dynamic species.

high β. For both 66404 and 73224, it was only necessary to maintain the perpendicular magnetic

Table 6. Same as Table 1 except for discharge 75225 with four dynamic species.

	$Q_e/Q_{e,gB}$	$Q_i/Q_{e,gB}$	$Q_{imp}/Q_{e,gB}$	$Q_{e,B\perp}/Q_{e,gB}$	$\Gamma_e/\Gamma_{e,gB}$	$\Gamma_i/\Gamma_{e,gB}$
GYRO	1.13 ± 0.16	3.75 ± 0.56	0.109 ± 0.01	—	0.42 ± 0.06	0.21 ± 0.03
GENE	0.91 ± 0.09	3.06 ± 0.29	0.093 ± 0.01	—	0.34 ± 0.03	0.17 ± 0.02

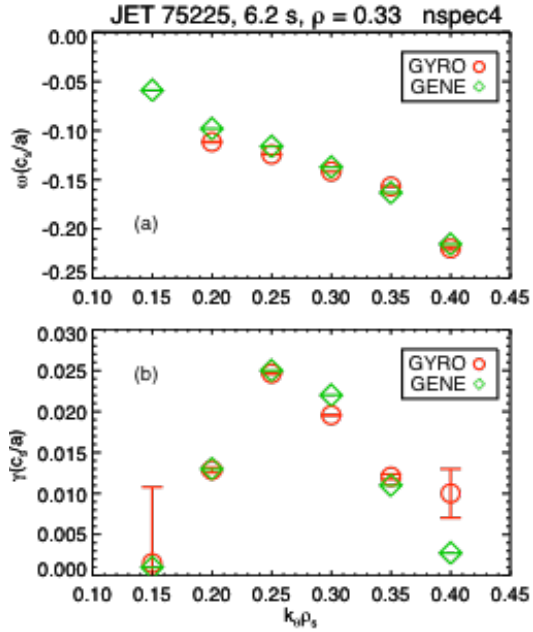

Figure 13. Same as Fig. 11 except electromagnetic.

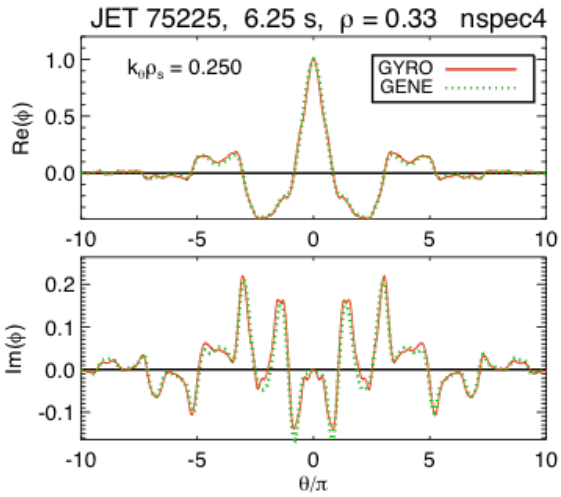

Figure 14. Same as Fig. 12 except electromagnetic.

Table 7. Same as Table 6 except electromagnetic.

	$Q_e/Q_{e,gB}$	$Q_i/Q_{e,gB}$	$Q_{imp}/Q_{e,gB}$	$Q_{e,B\perp}/Q_{e,gB}$	$\Gamma_e/\Gamma_{e,gB}$	$\Gamma_i/\Gamma_{e,gB}$
GYRO	< 0.002	< 0.002	< 0.002	< 0.002	< 0.002	< 0.002
GENE	0.05 ± 0.02	0.16 ± 0.04	0.004 ± 0.001	-0.002 ± 0.002	0.019 ± 0.007	0.012 ± 0.006

fluctuations

We first note the low values of the growth rates and fluxes. In fact, as seen in Fig. 13, the low-k_θ growth rates are non-zero over only a narrow range of $k_\theta\rho_s$. This is a difficult discharge to analyze owing to the fact that the plasma is near a KBM/BAE (kinetic ballooning mode / β-induced-Alfvèn-eigenmode) boundary. Furthermore, the GYRO nonlinear simulation is stable, i.e., the flux amplitudes never grow much beyond the initial noise levels. We should mention that slight adjustment (~10%) to driving terms, like a/L_{Ti}, or stabilizing terms like β can result in finite fluxes from GYRO. These results certainly point out the dominant role of electromagnetic stabilization.

Since the electromagnetic fluxes decay in time, we next examine electrostatically the role of **E×B** flow shear on this discharge. The results are shown in Table 8, where we see excellent agreement between the codes. Comparing with Table 6, we note only a modest reduction in the fluxes — not nearly as large as that from electrostatic to electromagnetic.

Conclusions

By comparing linear frequencies and fluxes from the GENE and GYRO gyrokinetic codes for three different discharges, we have seen that the reduction in fluxes due to electromagnetic effects is proportionately greater than the reductions in linear growth rates. Furthermore, as demonstrated in two of the discharges, electromagnetic effects play a more stabilizing effect than **E×B** flow shear. In the process, we have established that the two codes are in quantitative agreement on all these points. This is a significant result since benchmarking codes in high-performance multi-species electromagnetic regimes is rare in the literature. This is important for quasilinear code verification and extrapolations to low-rotation high-β reactors, among others.

Table 8. Same as Table 7 except including E×B flow shear.

	$Q_e/Q_{e,gB}$	$Q_i/Q_{e,gB}$	$Q_{imp}/Q_{e,gB}$	$Q_{e,B\perp}/Q_{e,gB}$	$\Gamma_e/\Gamma_{e,gB}$	$\Gamma_i/\Gamma_{e,gB}$
GYRO	0.87 ± 0.08	2.90 ± 0.27	0.103 ± 0.010	—	0.323 ± 0.029	0.122 ± 0.012
GENE	0.83 ± 0.075	2.69 ± 0.25	0.095 ± 0.007	—	0.306 ± 0.027	0.135 ± 0.015

Acknowledgements

This work was conducted under the auspices of the ITPA Topical Group on Transport and Confinement. Funding was provided through USDoE grant DE-FG02-08ER54978 and EUROfusion contract 633053.

References

[1] J. Weiland and A. Hirose, Nucl. Fusion **32** (1992) 151.

[2] A. Hirose, Phys. Plasmas **7** (2000) 433.

[3] M. Romanelli, A. Zocco, F. Crisanti and JET-EFDA Contributors, Plasma Phys. Control. Fusion **52** (2010) 045007.

[4] G. Falchetto et al., Phys. Plasmas **10** (2003) 1424.

[5] L. Villard et al., Nucl. Fusion **44** (2004) 172.

[6] M. J. Pueschel, M. Kammerer and F. Jenko Phys. Plasmas **15** (2008) 102310.

[7] M. J. Pueschel and F. Jenko Phys. Plasmas **17** (2010) 062307.

[8] M. J. Pueschel, T. Görler, F. Jenko, D. R. Hatch and A. J. Cianciara Phys. Plasmas **20** (2013) 102308.

[9] J. Citrin et al., Plasma Phys. Control. Fusion **57** (2015) 014032.

[10] J. Citrin et al., Nucl. Fusion **54** (2014) 023008.

[11] J. Citrin, F. Jenko, P. Mantica, D. Told, C. Bourdelle, J. Garcia, J.W. Haverkort, G. M. D. Hogeweij, T. Johnson, and M. J. Pueschel, Phys. Rev. Lett., **111** (2013) 155001.

[12] J. Citrin, J. Garcia, T. Görler, F. Jenko, P. Mantica, D. Told, C. Bourdelle, D R Hatch, G. M. D. Hogeweij, T. Johnson, M. J. Pueschel, M. Schneider and JET-EFDA Contributors, Plasma Phys. Contr. Fusion **57** (2015) 014032.

[13] J. Garcia et al., Nucl. Fusion **55** (2015) 053007.

[14] J. Candy, Phys. Plasmas **12** (2005) 072307.

[15] Y. Chen et al., Nucl. Fusion **43** (2003) 1121.

[16] C. Holland et al., Nucl. Fusion **52** (2012) 114007.

[17] F. Jenko, W. Dorland, M. Kotschenreuther, and B. N. Rogers, Phys. Plasmas **7** (2000) 1904.

[18] P. Mantica et al., Phys. Rev. Lett. **102** (2009) 175002.

[19] P Mantica et al., Phys. Rev. Lett. **104 (**2011) 135004.

[20] J. Y. Kim, W. Horton and J. Q. Dong 1993 Phys. Fluids B **5** (1993) 4030.

[21] J. Citrin et al., Plasma Phys. Control. Fusion **57** (2015) 014032.

[22] M. J. Pueschel, T. Görler, F. Jenko, D. R. Hatch and A. J. Cianciara Phys. Plasmas **20** (2013) 102308.

[23] J. Candy and R. E. Waltz, J. Comput. Phys. **186** (2003) 545.

[24] R. L. Miller, M. S. Chu, J. M. Greene, Y. R. Lin-Liu, and R. E. Waltz, Phys. Plasmas **5** (1998) 973; R. E. Waltz and R. L. Miller, *ibid*. **6** (1999) 4265; J. Candy, Plasma Phys. Controlled Fusion **51** (2009) 105009.